

RESEARCH ARTICLE

10.1002/2017JC013500

Key Points:

- New method to determine 2-D turbulent characteristics from a single Lagrangian drifter
- Effectiveness of using the empirical mode decomposition for the ocean community
- Mesoscale eddy characteristics in the California Current system identified from RAFOR floats

Correspondence to:

P. C. Chu,
pcchu@nps.edu

Citation:

Chu, P. C. (2018). Steepest ascent low/non-low-frequency ratio in empirical mode decomposition to separate deterministic and stochastic velocities from a single Lagrangian drifter. *Journal of Geophysical Research: Oceans*, 123, 1708–1721. <https://doi.org/10.1002/2017JC013500>

Received 26 SEP 2017

Accepted 15 JAN 2018

Accepted article online 25 JAN 2018

Published online 2 MAR 2018

Steepest Ascent Low/Non-Low-Frequency Ratio in Empirical Mode Decomposition to Separate Deterministic and Stochastic Velocities From a Single Lagrangian Drifter

Peter C. Chu¹ 

¹Naval Ocean Analysis and Prediction Laboratory, Department of Oceanography, Naval Postgraduate School, Monterey, CA, USA

Abstract SOUND Fixing And Ranging (RAFOS) floats deployed by the Naval Postgraduate School (NPS) in the California Current system from 1992 to 2001 at depth between 150 and 600 m (<http://www.oc.nps.edu/npsRAFOS/>) are used to study 2-D turbulent characteristics. Each drifter trajectory is adaptively decomposed using the empirical mode decomposition (EMD) into a series of intrinsic mode functions (IMFs) with corresponding specific scale for each IMF. A new steepest ascent low/non-low-frequency ratio is proposed in this paper to separate a Lagrangian trajectory into low-frequency (nondiffusive, i.e., deterministic) and high-frequency (diffusive, i.e., stochastic) components. The 2-D turbulent (or called eddy) diffusion coefficients are calculated on the base of the classical turbulent diffusion with mixing length theory from stochastic component of a single drifter. Statistical characteristics of the calculated 2-D turbulence length scale, strength, and diffusion coefficients from the NPS RAFOS data are presented with the mean values (over the whole drifters) of the 2-D diffusion coefficients comparable to the commonly used diffusivity tensor method.

Plain Language Summary A new method is presented to determine two-dimensional turbulent characteristics (length, strength, and diffusivity) from a single Lagrangian drifter rather than from a large group of Lagrangian drifters as the existing methods do.

1. Introduction

A Lagrangian drifter provides fluid characteristics along fluid particles' trajectories (i.e., Lagrangian trajectories), which make water masses distinguishable in terms of origin and/or destination and traced, while its characteristics are continually changing. Velocity can be calculated from Lagrangian trajectories using routine ocean data assimilation systems (e.g., Galanis et al., 2006; Sun et al., 2009) and data analysis methods such as optimal interpolation (OI; Melnichenko et al., 2016), and optimal spectral decomposition (OSD; Chu et al., 2003a, 2003b). Some phenomena were identified such as fall-winter recurrence of current reversal from westward to eastward on the Texas-Louisiana continental shelf from near-surface drifting buoy and current meter (Chu et al., 2005), and propagation of long baroclinic Rossby waves at middepth (around 1,000 m deep) in the tropical north Atlantic from the Argo floats (Chu et al., 2007).

Let $\{\mathbf{x}^{(n)}(t) = [x^{(n)}(t), y^{(n)}(t)], \mathbf{u}^{(n)}(x, y, t), n = 1, 2, \dots, N\}$ represent the time series of horizontal position (x zonal, y latitudinal) and velocity of N Lagrangian drifters at time t . How to identify currents and eddies from them has been studied for several decades with two major approaches. The first one is the particle dispersion relative to their center,

$$X(t) = \frac{1}{N} \sum_{n=1}^N x^{(n)}(t), \quad Y(t) = \frac{1}{N} \sum_{n=1}^N y^{(n)}(t). \quad (1)$$

The variances of locations of N drifters at time instance t ,

$$D_x(t) = \frac{1}{N} \sum_{n=1}^N [x^{(n)}(t) - X(t)]^2, \quad D_y(t) = \frac{1}{N} \sum_{n=1}^N [y^{(n)}(t) - Y(t)]^2 \quad (2)$$

estimate the dispersion of the drifters (e.g., Obuko & Ebbesmeyer, 1976; Rypina et al., 2012). The 2-D turbulent diffusivities (K_x, K_y) are defined by

$$K_x = \frac{1}{2} \frac{\partial D_x}{\partial t}, \quad K_y = \frac{1}{2} \frac{\partial D_y}{\partial t}. \quad (3)$$

With (D_x, D_y) grow linearly with time and the corresponding constant spreading rates (K_x, K_y) are referred as the 2-D turbulent diffusivity (Rypina et al., 2012).

The second approach is to estimate the Eulerian mean velocity from a group of N drifters,

$$\mathbf{U}(x, y) = \langle \mathbf{u}^{(n)}(x, y, t) \rangle,$$

and subtraction of $\mathbf{U}(x, y)$ from the velocity identified from Lagrangian drifters, $\mathbf{u}^{(n)}(x, y, t)$, leads to the “residue” velocities,

$$\mathbf{u}_{res}^{(n)}(x, y, t) = \mathbf{u}^{(n)}(x, y, t) - \mathbf{U}(x, y). \quad (4)$$

Here the Eulerian mean velocities are computed as an ensemble average in the defined geographic region that velocities from different floats and times (e.g., Collins et al., 2004; Chu et al., 2007, 2008; Chu & Fan, 2014; Davis, 1991) or as binned velocities with cubic splines (Bauer et al., 1998). This approach (a) requires well separation of the mean and residual velocities, (b) requires near Gaussian distribution of the residual velocities, (c) has possible false impression of diffusion gradient caused by nonuniform drifter coverage, and (d) has possible effect of mean velocity on the diffusivity. Interested readers may read a review paper by LaCasce (2008). Three methods are available to calculate the 2-D turbulent diffusivity from the Lagrangian residue velocities $[\mathbf{u}_{res}^{(n)}(x, y, t)]$ from a group of N drifters: (1) Lagrangian velocity autocorrelation (e.g., Paduan & Niiler 1993; Poulain & Niiler, 1989), (2) diffusivity tensor (Davis, 1991), and (3) minor principal component of the Davis’ diffusivity tensor (Zhurbas & Oh, 2003).

Both approaches (particle dispersion and Lagrangian residue velocities) need sufficient number (M) of drifters in the calculation. What should we do if there is very few codeployed drifters such as less than three RAFOS floats available at same time periods by the Naval Postgraduate School (NPS) in the California coasts (see website: <http://www.oc.nps.edu/npsRAFOS/>)? One option is to combine drifters from different time periods together as if they were deployed at the same time period.

Collins et al. (2004) calculated the diffusion coefficients for the California Current system from NPS floats N115, N108, N102 (not listed in the website), N090, N089, N088, N085, N071, N064, N050, and N039 between 1992 and 2002 using the diffusivity tensor method (Davis, 1991),

$$K_x = 920 \text{ m}^2/\text{s}, \quad K_y = 1,070 \text{ m}^2/\text{s}. \quad (5)$$

Other estimates are $(K_x = 3.4 \times 10^3 \text{ m}^2/\text{s}, K_y = 4.2 \times 10^3 \text{ m}^2/\text{s})$ from 124 drifters deployed 1985–1990 (Swenson & Niiler, 1996), $K = 3.8 \times 10^3 \text{ m}^2/\text{s}$ by Zhurbas and Oh (2003) using the diffusivity tensor with minor principle component. With the Lagrangian velocity autocorrelation, the diffusion coefficients are $(K_x = (3.4–4.1) \times 10^3 \text{ m}^2/\text{s}, K_y = (4.3–5.9) \times 10^3 \text{ m}^2/\text{s})$ from 29 TRISTAR-I drifters in the California Current system 1985–1986 (Poulain & Niiler, 1989), and $(K_x = (0.84–1.1) \times 10^3 \text{ m}^2/\text{s}, K_y = (1.5–1.6) \times 10^3 \text{ m}^2/\text{s})$ from 47 TRISTAR-II drifters in the northeast Pacific in October 1987 (Paduan & Niiler, 1993). Interested readers are referred to Zhurbas and Oh (2003, their Table 1).

A question arises: Can we determine 2-D turbulent diffusion coefficients from a single drift trajectory? The purposes here are to answer this question and to present a simple and effective method to do so on the base of the empirical mode decomposition (EMD; Huang et al., 1998; see Appendix A). The rest of the paper is organized as follows. Section 2 depicts the stochastic Lagrangian velocity and turbulent characteristics. Section 3 describes the EMD of Lagrangian trajectory. Section 4 introduces the low/non-low-frequency ratio for each IMF. Section 5 presents the steepest ascent low/non-low-frequency ratio to separate deterministic and stochastic velocities for each float. Sections 6 and 7 show 2-D turbulence length, strength, and diffusion coefficients for each float and their statistical characteristics. Section 8 presents the conclusions.

2. Stochastic Lagrangian Velocity

Let the position vector from a Lagrangian drifter at time instance t_j be represented by $\mathbf{x}(t_j) = [x(t_j), y(t_j)]$, $j = 1, 2, \dots, J$ with J the total number of the position points (or size of the time series). The two one-dimensional time series, $[x(t_j), y(t_j)]$ represent two-dimensional motion but not in the Eulerian sense since they are not

evaluated at all the grid points inside the domain of interest. Thus, the drifter position data $[x(t_j), y(t_j)]$ can only be individually analyzed as two separated univariate signals.

Let time series of position vector consist of low frequency (deterministic) $[\mathbf{x}_{det}(t_j)]$ (i.e., deterministic displacement) and high frequency (stochastic) $[\mathbf{x}_{sto}(t_j)]$ (i.e., stochastic displacement) components,

$$\mathbf{x}(t_j) = \mathbf{x}_{det}(t_j) + \mathbf{x}_{sto}(t_j), \quad j = 1, 2, \dots, J. \tag{6}$$

The deterministic and stochastic velocities (only showing stochastic) can be calculated from position vector (only showing x direction) with the first-order difference for the two endpoints,

$$u_{sto}(t_1) = \frac{x_{sto}(t_2) - x_{sto}(t_1)}{t_2 - t_1}, \quad u_{sto}(t_j) = \frac{x_{sto}(t_j) - x_{sto}(t_{j-1})}{t_j - t_{j-1}}, \tag{7}$$

and the central difference for the internal points,

$$u_{sto}(t_j) = \frac{x_{sto}(t_{j+1}) - x_{sto}(t_{j-1})}{t_{j+1} - t_{j-1}}, \quad j = 2, 3, \dots, J-1. \tag{8}$$

It is noted that the stochastic Lagrangian velocity, $\mathbf{u}_{sto}(t) = [u_{sto}(t), v_{sto}(t)]$, is not the same as the residual velocity $\mathbf{u}_{res}^{(n)}(x, y, t)$ defined by (4). The root mean squares of $[x_{sto}(t_j), y_{sto}(t_j)]$,

$$\delta_x = \sqrt{\frac{1}{J} \sum_{j=1}^J x_{sto}^2(t_j)}, \quad \delta_y = \sqrt{\frac{1}{J} \sum_{j=1}^J y_{sto}^2(t_j)} \tag{9}$$

represent the 2-D turbulence lengths. The root mean squares of $[u_{sto}(t_j), v_{sto}(t_j)]$,

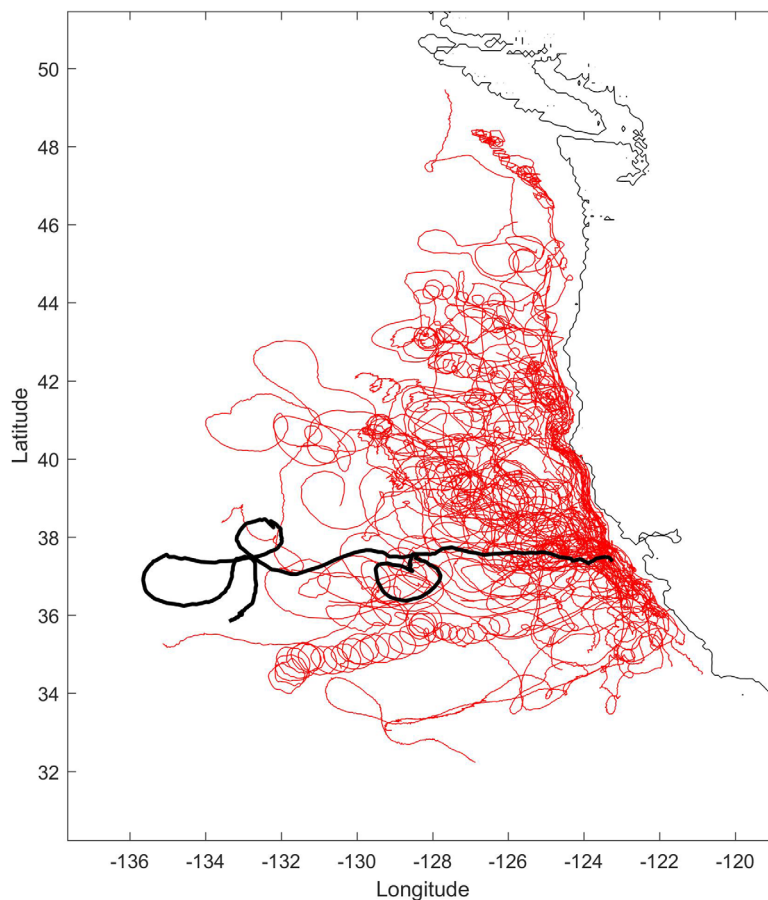


Figure 1. Trajectories of 54 RAFOS floats in the California coast by the Naval Postgraduate School between 1992 and 2004 (<http://www.oc.nps.edu/npsRAFOS/>). The thick black trajectory refers to the Float N035.

$$\sigma_x = \sqrt{\frac{1}{J} \sum_{j=1}^J u_{sto}^2(t_j)}, \quad \sigma_y = \sqrt{\frac{1}{J} \sum_{j=1}^J v_{sto}^2(t_j)} \quad (10)$$

represent the turbulence strengths. The 2-D turbulent diffusion coefficient is proportional to the product of turbulence length and strength on the base of Monin and Yaglom (1971)'s turbulence with mixing length theory,

$$K_x = c\sigma_u\delta_x, \quad K_y = c\sigma_v\delta_y, \quad (11)$$

where $c (=0.1)$ is the Ozmidov coefficient (Ozmidov, 1960). For given mixing lengths (δ_x, δ_y), turbulent diffusion increases with increasing turbulence strength (σ_u, σ_v). For given turbulence strength (σ_u, σ_v), turbulent diffusion increases with increasing mixing lengths (δ_x, δ_y). Thus, identification of stochastic displacement

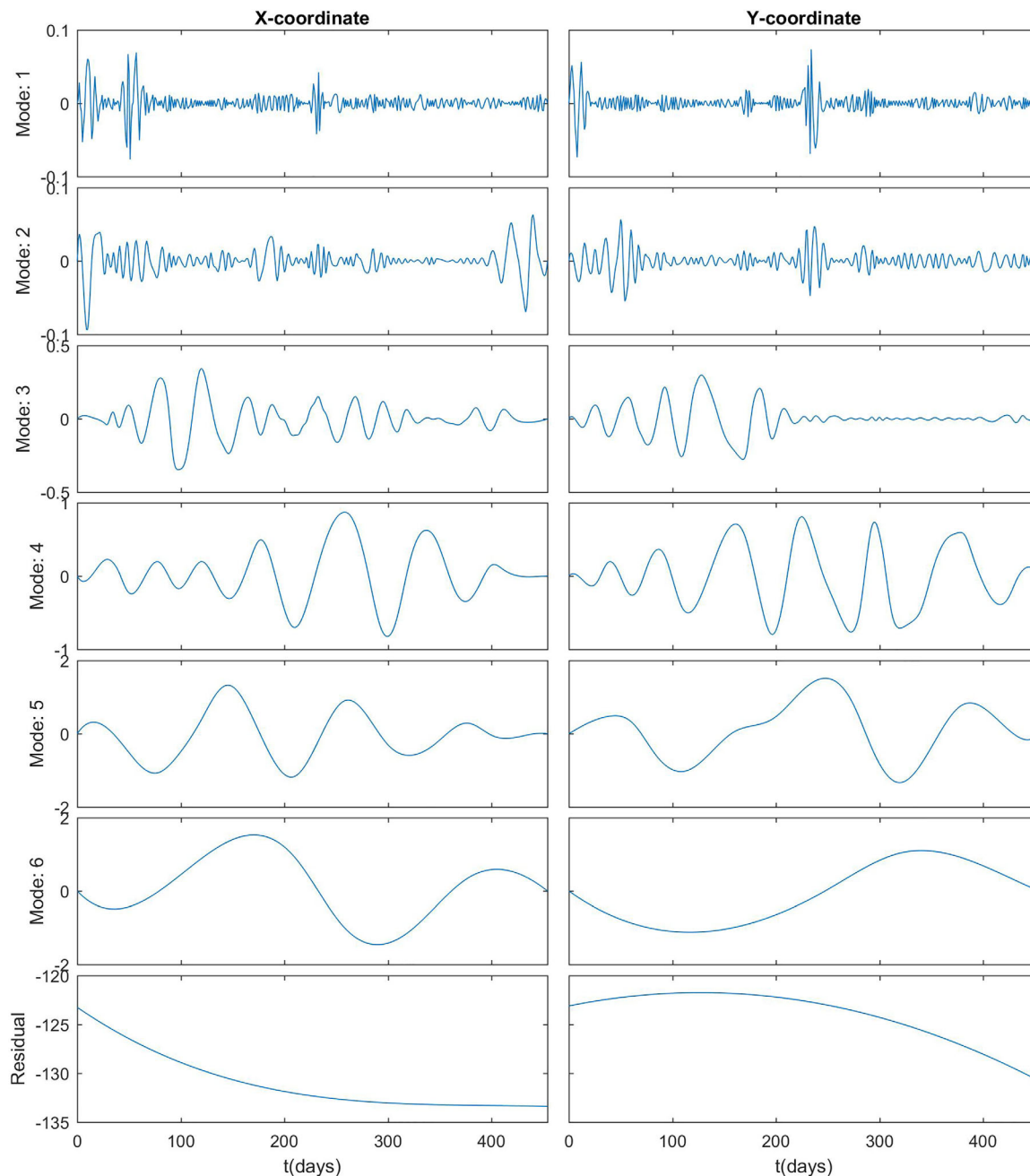


Figure 2. The IMFs and trend of (a) $x(t)$ and (b) $y(t)$ of the RAFOS float N035 from 7 August 1995 to 5 November 1996.

$[x_{sto}(t_j), y_{sto}(t_j), j = 1, 2, \dots, J]$ provides possibility to determine turbulent diffusion coefficients from a single Lagrangian drifter. Chu (2017) demonstrated such a possibility on the base of the empirical mode decomposition (EMD; Huang et al., 1998; see Appendix A), but he has not shown how to separate deterministic and stochastic motions from a drifter's trajectory.

3. EMD of Lagrangian Trajectory

The EMD supports the decomposition of signals into IMFs regardless of their linearity, stationarity, and stochasticity (e.g., Chu et al., 2012, 2014; Huang et al., 1998). The key point to perform this decomposition is the sifting process with four steps, which decompose a Lagrangian drift trajectory $\mathbf{x}(t)$ into (see equation (A5)),

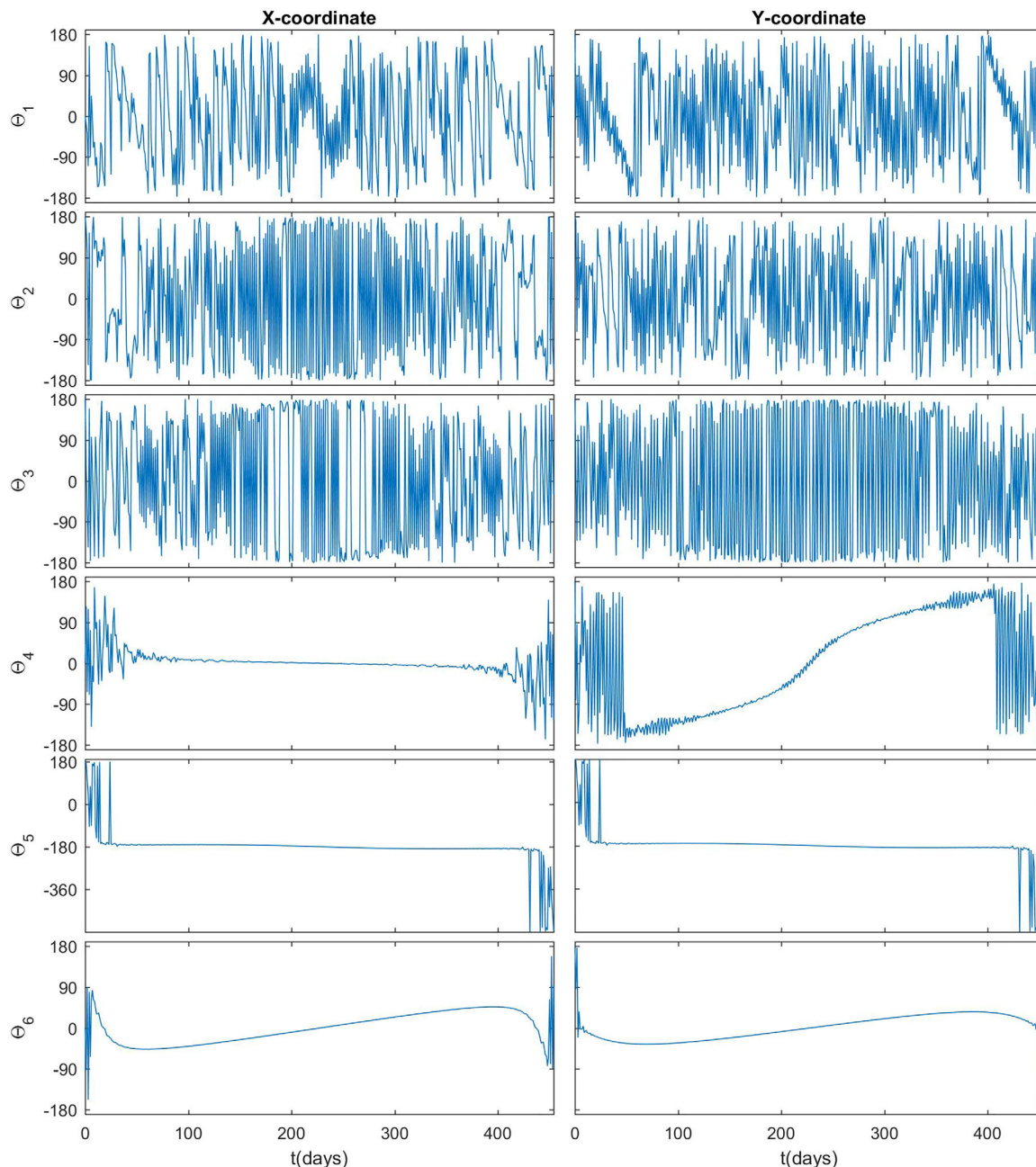


Figure 3. The phase spectra for the IMFs in Figure 2.

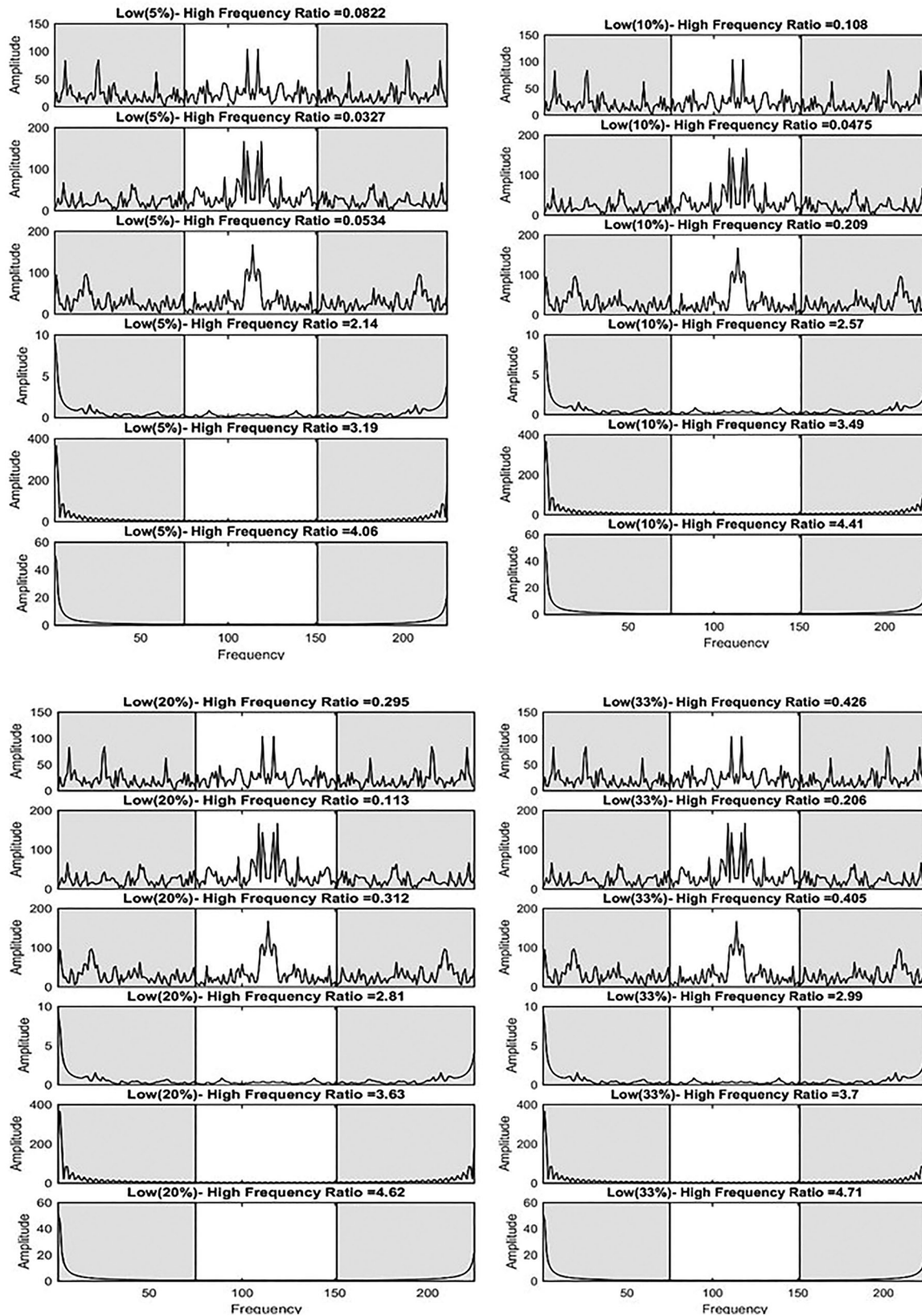


Figure 4. Fourier spectra and lowest (5%, 10%, 20%, and 33%)—high-frequency ratios for each IFM of the N035 RAFOS float from 7 August 1995 to 5 November 1996. The steepest ascent (6.736, 3.090, 2.282, and 1.889) occurs from IFM-3 to IFM-4. Thus, combination of IFM-4, IFM-5, IFM-6, and trend constitutes the deterministic component.

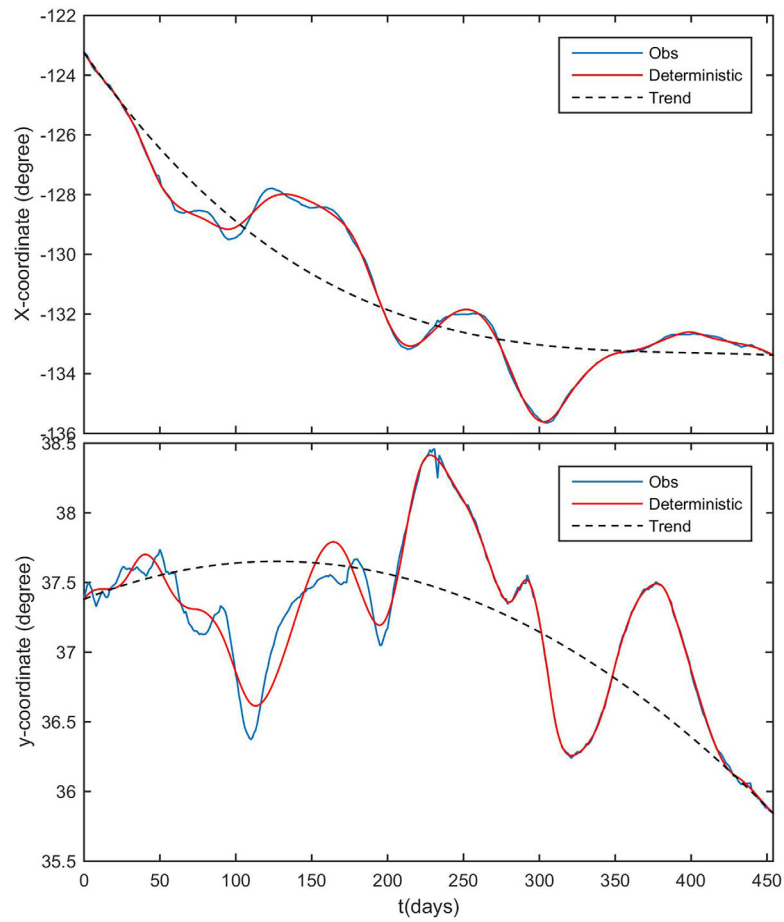


Figure 5. Comparison of RAFOS N035 among (a) $x(t)$, $x_d(t)$, $x_{trend}(t)$ and (b) $y(t)$, $y_d(t)$, $y_{trend}(t)$.

$$\mathbf{x}(t) = \sum_{p=1}^P \mathbf{x}_p(t) + \mathbf{r}(t), \tag{12}$$

where $\mathbf{x}_p(t) = [x_p(t), y_p(t)]$, is the p th IMF and $\mathbf{r}(t) = [r_x(t), r_y(t)]$ is the trend (not oscillated). The first IMF has highest frequency, and frequency reduces as the subscript p increases. The trajectory of NPS RAFOS float

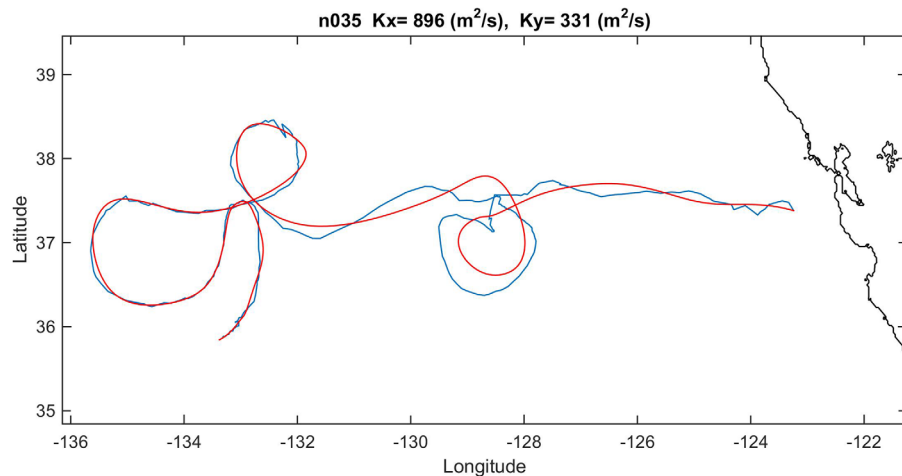


Figure 6. Observed (blue) and deterministic (red) trajectories of RAFOS N035.

Table 1
Low-Frequency Dominance Parameter $R_{p,z}$ and the Ascent Parameter $\Gamma_{p,z}$ for Each IMF of the N035 RAFOS Float From 7 August 1995 to 5 November 1996

IMF	$\alpha = 5\%$		$\alpha = 10\%$		$\alpha = 20\%$		$\alpha = 33\%$	
	$R_{p,z}$	$\Gamma_{p,z}$	$R_{p,z}$	$\Gamma_{p,z}$	$R_{p,z}$	$\Gamma_{p,z}$	$R_{p,z}$	$\Gamma_{p,z}$
1	0.0822	0.398	0.108	0.440	0.295	0.383	0.426	0.484
2	0.0327	1.633	0.0475	4.400	0.113	2.761	0.206	1.966
3	0.0534	40.075*	0.209	12.297*	0.312	9.006*	0.405	7.383*
4	2.14	1.491	2.57	1.358	2.81	1.292	2.99	1.237
5	3.19	1.273	3.49	1.264	3.63	1.273	3.70	1.273
6	4.06		4.41		4.62		4.71	

#N035 (thick curve in Figure 1), downloaded from <http://www.oc.nps.edu/npsRAFOS/DATAS/NPS035/DATAS.html>, is used for illustration. Six IFMs and a trend are identified in the (x, y) directions (Figure 2). It clearly shows that the high-frequency motion dominates the low IFM modes. Frequency reduces as the IFM mode from the lowest (IMF-1) to the highest (IMF-6). The trend (no oscillation) is of course the part of the deterministic motion, but not all. Rios and de Mello (2016) claimed that the IFMs can be combined to form additive deterministic and stochastic components. Summation of trend and deterministic IFMs constitute the deterministic motion (or deterministic Lagrangian trajectory).

4. Low/Non-Low-Frequency Ratio

The Fourier transform is conducted on each IMF $c_p(t)$ [$c_p(t)$ representing $x_p(t)$ and $y_p(t)$],

Table 2
2-D Turbulence Length Scales (δ_x, δ_y) Identified From Each RAFOS Float

Float	δ_x (m)	δ_y (m)	Float	δ_x (m)	δ_y (m)
N002	6,160	7,282	N050	107,415	118,217
N003	28,182	31,196	N051	188,122	61,380
N004	93,324	60,060	N053	117,579	86,823
N005	25,333	10,582	N055	83,039	123,343
N006	82,434	35,343	N062	108,559	76,252
N007	13,134	22,253	N063	66,121	44,627
N008	18,304	17,743	N064	134,970	48,906
N010	41,173	27,588	N065	25,025	21,604
N011	17,226	16,445	N066	117,150	121,286
N013	34,430	28,512	N067	126,951	110,616
N014	41,448	29,579	N069	106,392	59,345
N019	72,666	98,307	N071	32,626	55,165
N021	1,738	638	N072	95,964	106,733
N022	825	737	N073	37,598	31,944
N024	2,640	781	N075	125,422	108,284
N026	61,468	17,853	N080	154,682	152,262
N028	32,505	16,654	N081	141,251	146,927
N029	19,811	27,775	N082	67,331	80,718
N030	946	18,678	N083	111,694	129,591
N031	82,357	65,340	N084	158,752	120,054
N032	57,002	52,305	N085	120,439	149,622
N033	22,451	78,551	N087	101,871	160,204
N035	129,514	54,351	N088	96,162	229,647
N039	107,481	104,852	N089	139,667	224,103
N041	149,039	91,839	N090	179,487	250,008
N043	106,986	68,706	N091	149,611	152,449
N048	92,103	18,579	N092	134,596	141,218

$$f_{pk} = \frac{1}{J} \sum_{t=0}^{J-1} c_p(t) \exp [(-i2\pi k/J)t], \quad k=0, 2, \dots, J-1, \quad (13)$$

which is a set of complex coefficients in frequency space. Here $i \equiv \sqrt{-1}$ and T is the length of the time series. For each IFM, $c_p(t)$ the phase spectrum (Rios & de Mello, 2016) of is calculated by

$$\theta_p(k) = \arctan \frac{\text{Im}(f_{pk})}{\text{Re}(f_{pk})} \quad (14)$$

and the amplitude is computed up to the Nyquist frequency

$$a_p(k) = \sqrt{|f_{pk} \hat{f}_{pk}|} / J, \quad k=1, 2, \dots, J/2. \quad (15)$$

Let m represents lowest α -fraction ($\alpha < 1$) of the frequency domain, i.e., $m = [\alpha \times J/2]$ with the bracket indicating the integer part. The powers of lowest α -fraction frequency (E_{α}) and total frequency (E_T) are defined by

$$E_{p,\alpha} = \sum_{k=1}^m a_p^2(k), \quad E_{p,T} = \sum_{k=1}^{J/2} a_p^2(k). \quad (16)$$

The low/non-low-frequency ratio is defined by

$$R_{p,\alpha} = \frac{E_{p,\alpha}}{E_{p,J} - E_{p,\alpha}}, \quad (17)$$

which indicates the low-frequency (α -fraction) dominance of the p th IMF.

5. Steepest Ascent Low/Non-Low-Frequency Ratio

The ratio of the low-frequency dominance parameter for the $(p + 1)$ th IMF to the p th IMF,

$$\Gamma_{p,\alpha} = \frac{R_{p+1,\alpha}}{R_{p,\alpha}} \quad (18)$$

represents increase of strength of the low-frequency component. Since the low frequency enhances as the mode number p increases, separation of deterministic and stochastic signals is at the IMF with the maximum value of the ratio,

$$\Gamma_{s,\alpha} = \max(\Gamma_{p,\alpha} | p=1, 2, \dots, P-1). \quad (19)$$

The combination of the first, second, . . . , s th IMFs constitutes the stochastic signal, and the combination of $(s + 1)$ th, $(s + 2)$ th, . . . , P th IMFs, and the trend constitutes the deterministic signal.

Fourier transform is applied to all the 6 IMFs of the Float N035 in Figure 2, $[(x_p(t), y_p(t)), p = 1, 2, \dots, 6]$. The phase spectra show the frequency reduction for consecutive IMFs (Figure 3). The low-frequency dominance parameter ($R_{p,\alpha}$) and the parameter ratio ($\Gamma_{p,\alpha}$) are calculated for all the IMFs and four values of $\alpha = (0.05, 0.10, 0.20, 0.33)$ [see (15)–(17)]. For a particular α , $\Gamma_{3,\alpha}$ is the maximum among the five parameter ratios: 40.075 for $\alpha = 5\%$, 12.297 for $\alpha = 10\%$, 9.006 for $\alpha = 20\%$, and 7.383 for $\alpha = 33\%$ (see Figure 4 and Table 1). The values of $\Gamma_{4,\alpha}$ and $\Gamma_{5,\alpha}$ change from 1.237 ($\alpha = 33\%$) to 1.491 ($\alpha = 33\%$), i.e., minor change of the low/non-low-frequency ratio. Thus, the combination of first, second, and third IMFs constitutes stochastic velocities; the combination of fourth, fifth, and sixth IMFs and the trend

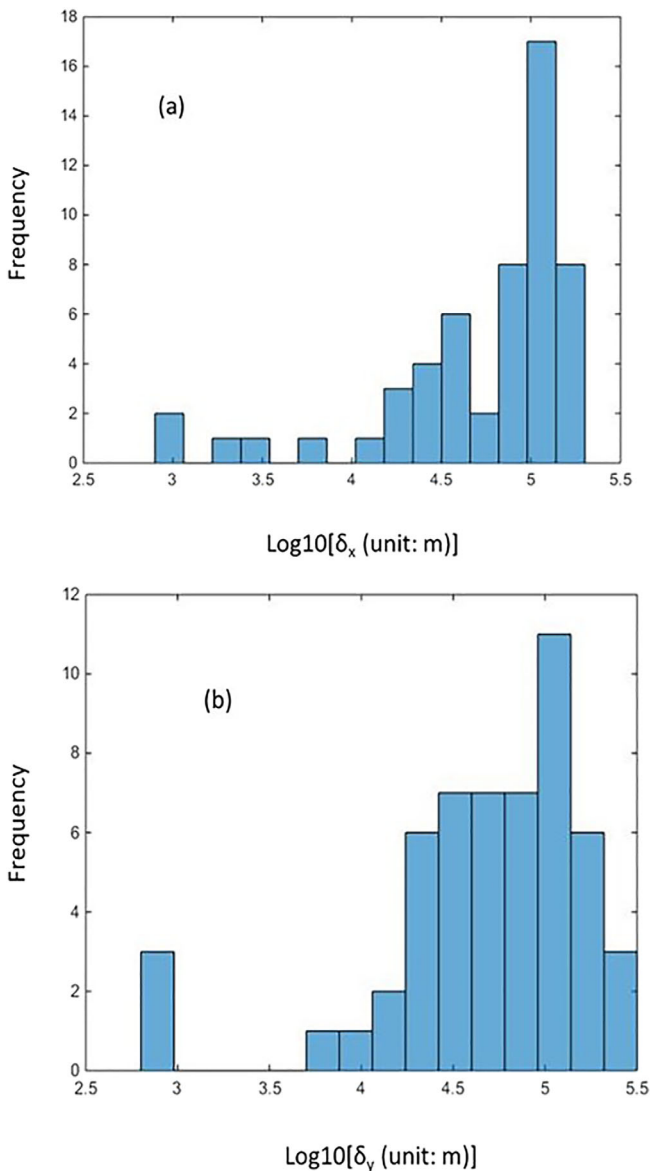


Figure 7. Histograms of 2-D turbulence length scales (a) δ_x and (b) δ_y (unit: m) identified from 54 RAFOS floats in the California coast by C. A. Collins at the Naval Postgraduate School from 1992 to 2001.

constitutes the deterministic velocities. Two position vectors, $\mathbf{x}_{det}(t) = [x_{det}(t), y_{det}(t)]$ and $\mathbf{x}_{trend}(t) = [x_{trend}(t), y_{trend}(t)]$, are constructed and compared to the original position vector $\mathbf{x}(t)$. The three time series in the two directions $[x(t), x_{det}(t), x_{trend}(t)]$ (Figure 5a) and $[y(t), y_{det}(t), y_{trend}(t)]$ (Figure 5b) and the trajectories of the three position vectors (Figure 6) show the separation of the deterministic and stochastic signals. It is clearly indicates that the trends $[x_{trend}(t), y_{trend}(t)]$ do not fully represent the deterministic signal. Here $\alpha = 10\%$ is used for the rest of the NPS RAFOS floats.

6. 2-D Turbulence Length and Strength

The RAFOS subsurface data downloaded from <http://www.oc.nps.edu/npsRAFOS/> contains 61 RAFOS floats. Among them seven floats (N001, N009, N012, N042, N046, N049, and N068) have too many missing data inside the time series. They are not included in the computation. The data rate varies from general 3/day to around 22/day (N030 18 May to 10 June 1994). For each float, the time series $[x(t_j), y(t_j)]$ are decomposed into IMFs and trend using the EMD method (see Appendix A). The method depicted in sections 4 and 5 is used to separate the deterministic and stochastic motion and to get $[x_{sto}(t_j), y_{sto}(t_j)]$ (see (6)) and $[u_{sto}(t_j), v_{sto}(t_j)]$ (see (7) and (8)). The 2-D turbulence length scales (δ_x, δ_y) are calculated using (9) and strengths (σ_x, σ_y) are calculated using (10).

Table 2 lists (δ_x, δ_y) for each of the 54 RAFOS floats. The averaged 2-D turbulence length scales are quite comparable in zonal (mean $(\delta_x) \sim 80.9$ km) and latitudinal (mean $(\delta_y) \sim 76.2$ km) directions. However, the length scales (δ_x, δ_y) identified from individual RAFOS floats are quite diverse with minima (825 m, 638 m), maxima (188.1 km, 250.0 km), standard deviations (52.1 km, 60.8 km), skewness (0.0439, 0.9350), and kurtosis (1.8801, 3.4033) (also see second and third rows of Table 5).

The histogram of $\log_{10} \delta_x$ (Figure 7a) shows that 33 RAFOS floats (61% of total floats) are in the three highest bins, i.e.,

Table 3
2-D Turbulence Strengths (σ_x, σ_y) Identified From Each RAFOS Float

Float	σ_x (cm/s)	σ_y (cm/s)	Float	σ_x (cm/s)	σ_y (cm/s)
N002	8.17	4.86	N050	7.51	7.36
N003	7.15	8.21	N051	7.60	7.00
N004	13.59	16.01	N053	6.33	6.54
N005	20.22	15.23	N055	6.93	10.27
N006	14.01	13.90	N062	4.86	5.98
N007	10.69	14.48	N063	4.01	3.56
N008	12.55	7.68	N064	6.35	6.50
N010	6.69	8.68	N065	9.44	3.62
N011	14.46	14.81	N066	7.93	6.73
N013	11.70	11.62	N067	8.77	9.63
N014	8.62	10.51	N069	5.10	4.31
N019	7.30	7.05	N071	2.76	3.94
N021	38.49	21.34	N072	5.63	4.36
N022	18.28	13.95	N073	13.46	13.51
N024	17.71	12.89	N075	9.49	10.43
N026	12.82	10.12	N080	7.24	6.91
N028	9.26	8.78	N081	6.51	7.61
N029	6.47	8.19	N082	10.26	11.07
N030	21.53	23.48	N083	10.89	11.85
N031	16.66	20.72	N084	4.84	5.69
N032	6.59	5.44	N085	8.07	9.07
N033	4.74	8.43	N087	5.93	5.65
N035	6.92	6.08	N088	5.08	5.76
N039	5.02	6.03	N089	5.46	11.51
N041	7.54	7.36	N090	10.05	8.27
N043	9.89	9.01	N091	6.23	5.50
N048	5.17	4.65	N092	7.20	9.05

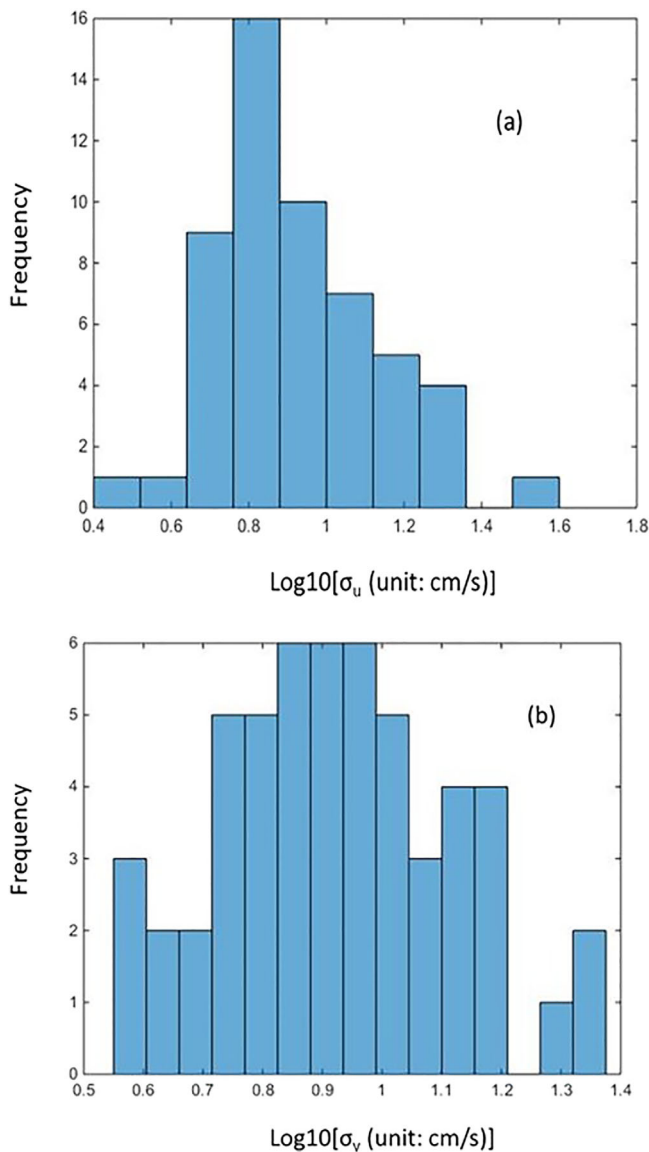


Figure 8. Histograms of 2-D turbulence strengths (a) σ_x and (b) σ_y (unit: cm/s) identified from 54 RAFOS floats in the California coast by C. A. Collins at the Naval Postgraduate School from 1992 to 2001.

$$67,608 \text{ m} = 10^{4.83} \text{ m} \leq \delta_x \leq 10^{5.33} \text{ m} = 213,796 \text{ m}.$$

Five RAFOS floats (9% of total floats) are in the lowest bins with δ_x less than 10 km (on submesoscale), and 16 RAFOS floats (30% of total floats) are between 10 and 67.6 km. The histogram of $\log_{10} \delta_y$ (Figure 7b) shows more spread out that 49 RAFOS floats (91% of total floats) represent mesoscale,

$$\delta_y \geq 10^4 \text{ m},$$

and 5 RAFOS floats (9% of total floats) are in the lower bins with δ_y less than 10 km (on submesoscale). Most (91%) of the stochastic parts of the RAFOS float trajectories represent the mesoscale motion.

Table 3 lists (σ_u, σ_v) for each of the 54 RAFOS floats. The averaged 2-D turbulence velocity scales are quite comparable in zonal (mean $(\sigma_u) \sim 9.58 \text{ cm/s}$) and latitudinal (mean $(\sigma_v) \sim 9.27 \text{ cm/s}$) directions. However, the turbulence velocity scales (σ_u, σ_v) identified from individual RAFOS floats are quite diverse with minima (2.76 cm/s, 3.56 cm/s), maxima (38.49 cm/s, 23.48 cm/s), standard deviations (5.80 cm/s, 4.46 cm/s), skewness (2.6760, 1.2684), and kurtosis (12.8330, 4.4720) (also see fourth, and fifth rows of Table 5).

The histogram of $\log_{10} \sigma_u$ (Figure 8a) shows that 51 RAFOS floats (94% of total floats) are in the range of

$$4.37 \text{ cm/s} = 10^{0.64} \text{ cm/s} \leq \sigma_u \leq 10^{1.36} \text{ cm/s} = 22.91 \text{ cm/s}.$$

Thirty-five RAFOS floats (65% of total floats) are in the three highest bins, i.e.,

$$4.37 \text{ cm/s} = 10^{0.64} \text{ cm/s} \leq \sigma_u \leq 10 \text{ cm/s}.$$

Two RAFOS floats (3.7% of total floats) are in the lowest bins with σ_u less than 4.37 cm/s, and 1 RAFOS float (1.9% of total floats) with σ_u higher than 22.91 cm/s, which is 38.49 cm/s from N021.

The histogram of $\log_{10} \sigma_v$ (Figure 8b) shows more spread out than σ_u that 44 RAFOS floats (81% of total floats) are in the range of

$$5.25 \text{ cm/s} = 10^{0.72} \text{ cm/s} \leq \sigma_v \leq 10^{1.22} \text{ cm/s} = 16.60 \text{ cm/s}.$$

7. Diffusion Coefficients

With given (δ_x, δ_y) and (σ_x, σ_y) , the diffusion coefficients (K_x, K_y) are computed using equation (11) for each RAFOS float. Table 4 lists (K_x, K_y) for each of the 54 RAFOS floats. The averaged 2-D turbulent diffusion coefficients are quite comparable in zonal (mean $(K_x) \sim 635 \text{ m}^2/\text{s}$) and latitudinal (mean $(K_y) \sim 629 \text{ m}^2/\text{s}$) directions. However, the diffusion coefficients (K_x, K_y) identified from individual RAFOS floats are quite diverse with minima (15 m^2/s , 10 m^2/s), maxima (1,803 m^2/s , 2,579 m^2/s), standard deviations (427 m^2/s , 536 m^2/s), skewness (0.4357, 1.3539), and kurtosis (2.5183, 5.1195) (also see sixth, and seventh rows of Table 5).

The histogram of $\log_{10} K_x$ (Figure 9a) shows that 45 RAFOS floats (83% of total floats) are in the range of

$$200 \text{ m}^2/\text{s} = 10^{2.30} \text{ m}^2/\text{s} \leq K_x \leq 1,803 \text{ m}^2/\text{s}.$$

Thirty-five RAFOS floats (65% of total floats) are in the four highest bins, i.e.,

Table 4
Horizontal Diffusivity Coefficients (K_x , K_y) Identified From Each RAFOS Float

Float	K_x (m ² /s)	K_y (m ² /s)	Float	K_x (m ² /s)	K_y (m ² /s)
N002	50.33	35.36	N050	807.00	869.98
N003	201.50	256.01	N051	1,428.79	429.88
N004	1,268.10	961.34	N053	744.84	567.72
N005	512.28	161.15	N055	575.79	1,266.25
N006	1,154.57	491.32	N062	527.90	455.62
N007	140.41	322.12	N063	264.97	159.00
N008	229.77	136.26	N064	857.32	317.78
N010	275.39	239.34	N065	236.35	78.13
N011	249.02	243.60	N066	928.46	816.23
N013	402.84	331.44	N067	1,113.50	1,064.76
N014	357.15	310.99	N069	542.80	255.66
N019	530.12	692.70	N071	90.03	217.50
N021	66.89	13.61	N072	540.54	464.90
N022	15.08	10.28	N073	506.08	431.43
N024	46.75	10.07	N075	1,190.04	1,128.97
N026	788.09	180.61	N080	1,119.79	1,052.69
N028	301.14	146.19	N081	919.83	1,118.54
N029	128.14	227.37	N082	690.91	893.65
N030	20.37	438.64	N083	1,216.25	1,535.29
N031	1,372.19	1,354.11	N084	768.98	683.10
N032	375.76	284.72	N085	971.53	1,357.00
N033	106.38	662.16	N087	604.49	904.98
N035	896.11	330.70	N088	488.44	1,323.34
N039	539.05	631.89	N089	762.60	2,579.02
N041	1,123.98	619.72	N090	1,803.36	2,067.87
N043	1,057.78	618.90	N091	931.87	838.59
N048	476.43	86.36	N092	969.12	1,277.95

$$407 \text{ m}^2/\text{s} = 10^{2.61} \text{ m}^2/\text{s} \leq K_x \leq 10^{3.22} \text{ m}^2/\text{s} = 1,660 \text{ m}^2/\text{s}.$$

Nine RAFOS floats (17% of total floats) are in the lower bins with K_x less than 141 ($=10^{2.15}$) m²/s, and 1 RAFOS float (1.9% of total floats) with K_x higher than 1,660 m²/s, which is 1,803 m²/s from N090.

The histogram of $\log_{10} K_y$ (Figure 9b) shows that 44 RAFOS floats (81% of total floats) are in the range of

$$200 \text{ m}^2/\text{s} = 10^{2.30} \text{ m}^2/\text{s} \leq K_y \leq 1,803 \text{ m}^2/\text{s}.$$

Eight RAFOS floats (15% of total floats) are in the lower bins with $K_y < 200$ m²/s, and 2 RAFOS floats (4% of total floats) higher bins with $K_y > 1,803$ m²/s, which are 2,579 m²/s for N089 and 2,068 m²/s for N090.

8. Conclusions

A new method is presented in this paper to separate deterministic and stochastic signals and to estimate the 2-D turbulent diffusion coefficients from a single Lagrangian drifter using steepest ascent low/non-low-

Table 5
Statistical Characteristics of 2-D Turbulence Length Scales, Strengths, and Diffusion Coefficients

	Mean	Min	Max	Standard deviation	Skewness	Kurtosis
δ_x	80,910 m	825 m	188,122 m	52,136 m	0.0439	1.8801
δ_y	76,183 m	638 m	250,008 m	60,832 m	0.9350	3.4033
σ_u	9.58 cm/s	2.76 cm/s	38.49 cm/s	5.80 cm/s	2.6760	12.8330
σ_v	9.27 cm/s	3.56 cm/s	23.48 cm/s	4.46 cm/s	1.2684	4.4720
K_x	634.95 m ² /s	15.08 m ² /s	1,803.36 m ² /s	426.83 m ² /s	0.4357	2.5183
K_y	628.76 m ² /s	10.07 m ² /s	2,579.02 m ² /s	535.96 m ² /s	1.3539	5.1195

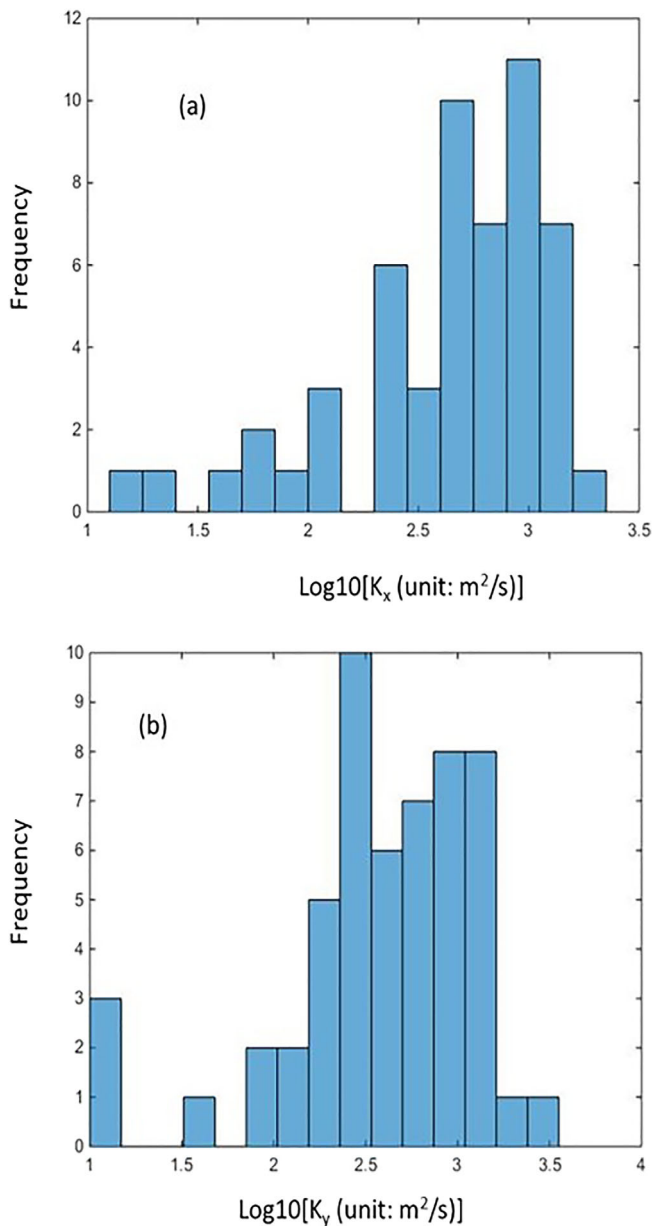


Figure 9. Histograms of turbulence diffusion coefficients (a) K_x and (b) K_y (unit: m^2/s) identified from 54 RAFOS floats in the California coast by C. A. Collins at the Naval Postgraduate School from 1992 to 2001.

It is subtracted from the original signal and the first residual,

$$r_1(t) = x(t) - h_1(t) \tag{A4}$$

is taken as the new series in step 1. If $h_1(t)$ is not an IMF, a procedure called “sifting process” is applied as many times as necessary to obtain an IMF. In the sifting process, $h_1(t)$ is considered as the new data, and the same procedure applies. The IMFs are orthogonal, or almost orthogonal functions (mutually uncorrelated). This method does not require stationarity and linearity of the data and is especially suitable for non-stationary and nonlinear time series analysis.

By construction, the number of extrema decreases when going from one residual to the next; the above algorithm ends when the residual has only one extrema, or is constant, and in this case no more IMF can be extracted; the complete decomposition is then achieved in a finite number of steps. The signal $x(t)$ is finally written as the sum of IMFs $c_p(t)$ and the trend $r(t)$:

frequency ratio in EMD and classical turbulence theory with mixing length theory. The calculated diffusion coefficients for the California Current system near Monterey are comparable using this method to the diffusivity tensor calculation (Collins et al., 2004).

Comparison between Tables 4 and 5 with Zhurbas and Oh (2003, Table 1) leads to the fact that the diffusion coefficients obtained using this method is comparable to Paduan and Niiler (1993) but lower than Poulain and Niiler (1989), Swenson and Niiler (1996), and Zhurbas and Oh (2003). The difference in the diffusion coefficients is caused by only one drifter used in this new method rather than an ensemble of drifters used in the existing methods.

This study also shows the capability of EMD to decompose the drifter’s trajectory with frequency reduction from IMF-1 to IMF-P (the last IMF) along IMF extraction. The low/non-low-frequency ratio (see section 4) represents the low-frequency dominance for each IMF. Its steepest ascent low/non-low-frequency ratio indicates refers to the separation of high-frequency (stochastic) and low-frequency (deterministic) signals. Such a separation is not sensitive to the selection of α (5%–33%) because of the frequency reduction along IMF extraction. This method can be used in general signal processing.

Appendix A: Empirical Mode Decomposition

This appendix is duplicated from Chu et al. (2012, section 2). Let $x(t)$ represent the time series with fluctuations on various time scales (see Chu et al., 2012, Figure 1). The EMD method is depicted as follows. First, the local minima and maxima of the signal $x(t)$ are identified. Second, the local maxima are connected together by a cubic spline interpolation (other interpolations are also possible), forming an upper envelope $e_{max}(t)$. The same is done for local minima, providing a lower envelope $e_{min}(t)$. Third, the mean of the two envelopes are calculated.

$$m_1(t) = [e_{max}(t) + e_{min}(t)]/2. \tag{A1}$$

Fourth, the mean is subtracted from the signal, providing the local detail

$$h_1(t) = x(t) - m_1(t), \tag{A2}$$

which is then considered to check if it satisfies the above two conditions to be an IMF. If yes, it is considered as the first IMF and denoted.

$$c_1(t) = h_1(t). \tag{A3}$$

$$x(t) = \sum_{p=1}^P c_p(t) + r(t). \quad (A5)$$

There is no any oscillation (i.e., nonexistence of both maximum and minimum envelopes) in the trend $r(t)$, which should represent the trend. Obviously, successfulness of the EMD depends on accurate determination of upper and lower envelopes.

Acknowledgments

The author thanks Curt Collins at NPS for collecting RAFOS data and unselfishly providing data at the website (<http://www.oc.nps.edu/npsRAFOS/>) and Chenwu Fan for his outstanding efforts on the computation and graphics.

References

- Bauer, S., Swenson, M. S., Griffa, A., Mariano, A. J., & Owens, K. (1998). Eddy-mean decomposition and eddy-diffusivity estimates in the tropical Pacific Ocean. *Journal of Geophysical Research*, *103*, 30855–30871.
- Chu, P. C. (2017). *Hilbert-Huang transform to estimate turbulent diffusion coefficient from a single Lagrangian drifter trajectory*. Paper presented at The 49th Liege Colloquium on Ocean Dynamics—The 8th Warnemunde Turbulence Days, Liege, Belgium, May 22–26, 2017.
- Chu, P. C., & Fan, C. W. (2014). Accuracy progressive calculation of Lagrangian trajectory from gridded velocity field. *Journal of Atmospheric and Oceanic Technology*, *31*(7), 1615–1627.
- Chu, P. C., Fan, C. W., & Huang, N. (2012). Compact empirical mode decomposition—An algorithm to reduce mode mixing, end effect, and detrend uncertainty. *Advances in Adaptive Data Analysis*, *4*(3), 1250017–1250018. <https://doi.org/10.1142/S1793536912500173>
- Chu, P. C., Fan, C. W., & Huang, N. (2014). Derivative-optimized empirical mode decomposition for the Hilbert-Huang transform. *Journal of Computational and Applied Mathematics*, *259*, 57–64.
- Chu, P. C., Ivanov, L. M., Korzhova, T. P., Margolina, T. M., & Melnichenko, O. M. (2003a). Analysis of sparse and noisy ocean current data using flow decomposition. Part 1: Theory. *Journal of Atmospheric and Oceanic Technology*, *20*(4), 478–491.
- Chu, P. C., Ivanov, L. M., Korzhova, T. P., Margolina, T. M., & Melnichenko, O. M. (2003b). Analysis of sparse and noisy ocean current data using flow decomposition. Part 2: Application to Eulerian and Lagrangian data. *Journal of Atmospheric and Oceanic Technology*, *20*(4), 492–512.
- Chu, P. C., Ivanov, L. M., & Melnichenko, O. M. (2005). Fall-winter current reversals on the Texas-Louisiana continental shelf. *Journal of Physical Oceanography*, *35*, 902–910.
- Chu, P. C., Ivanov, L. M., Melnichenko, O. V., & Li, R.-F. (2008). Argo floats revealing bimodality of large-scale mid-depth circulation in the North Atlantic. *Acta Oceanologica Sinica*, *27*(2), 1–10.
- Chu, P. C., Ivanov, L. M., Melnichenko, O. V., & Wells, N. C. (2007). On long baroclinic Rossby waves in the tropical North Atlantic observed from profiling floats. *Journal of Geophysical Research*, *112*, C05032. <https://doi.org/10.1029/2006JC003698>
- Collins, C. A., Ivanov, L. M., Melnichenko, O. B., & Gartfield, N. (2004). California undercurrent variability and eddy transport estimated from RAFOS float observations. *Journal of Geophysical Research*, *109*, C05028. <https://doi.org/10.1029/2003JC002191>
- Davis, R. E. (1991). Observing the general circulation with floats. *Deep Sea Research Part A. Oceanographic Research Papers*, *38*, S531–S571.
- Galanis, G. N., Louka, P., Katsafados, K. P. G., & Pytharoulis, I. (2006). Applications of Kalman filters based on non-linear functions to numerical weather predictions. *Annals of Geophysics*, *24*, 2451–2460.
- Huang, N., Shen, Z., Long, S. R., Wu, M. C., Smith, H. H., Zheng, Q., et al. (1998). The empirical mode decomposition and the Hilbert spectrum for nonlinear and non-stationary time series analysis. *Proceedings of the Royal Society of London, Series A: Mathematical, Physical and Engineering Sciences*, *454*, 903–995.
- LaCasce, J. H. (2008). Statistics from Lagrangian observations. *Progress in Oceanography*, *77*, 1–29.
- Melnichenko, O. V., Hacker, P., Maximenko, N. A., Lagerloef, G., & Potemra, J. T. (2016). Optimum interpolation analysis of Aquarius Sea surface salinity. *Journal of Geophysical Research: Oceans*, *121*, 602–616. <https://doi.org/10.1002/2015JC011343>
- Monin, A. S., & Yaglom, A. M. (1971). In J. L. Lumley (Ed.), *Statistical fluid mechanics. Mechanics of turbulence* (Vol. 1). Cambridge, MA: MIT Press. Translated from the Russian edition (Moscow, 1965), as revised by the authors.
- Obuko, A., & Ebbesmeyer, C. C. (1976). Determination of vorticity, divergence, and deformation rates from analysis of drogoue observations. *Deep Sea Research and Oceanographic Abstracts*, *23*(4), 349–352.
- Ozmidov, R. V. (1960). On rate of dissipation of turbulent energy in sea currents and on the dimensionless universal constant in the 4/3 power law. *Izvestia Akademii Nauk SSSR, Geophysical Series*, *8*, 1234–1237.
- Paduan, P. D., & Niiler, P. P. (1993). Structure of velocity and temperature in the northeast Pacific as measured with Lagrangian drifters in fall 1987. *Journal of Physical Oceanography*, *23*, 585–600.
- Poulain, P.-M., & Niiler, P. P. (1989). Statistical analysis of the surface circulation in the California Current system using satellite-tracked drifters. *Journal of Physical Oceanography*, *19*, 1588–1603.
- Rios, R. A., & de Mello, R. F. (2016). Applying empirical mode decomposition and mutual information to separate stochastic and deterministic influences embedded in signals. *Signal Processing*, *118*, 159–176.
- Rypina, I. I., Kamenkovich, I., Berloff, P., & Pratt, L. I. (2012). Eddy-induced particle dispersion in the near-surface North Atlantic. *Journal of Physical Oceanography*, *42*, 2206–2228.
- Sun, L. C., Thresher, A., Keeley, R., Hall, N., Hamilton, M., Chinn, P., et al. (2009). *The data management system for the Global Temperature and Salinity Profile Program (GTSPP)*. Paper presented at the Proceedings of the “OceanObs’09: Sustained Ocean Observations and Information for Society” Conference (Vol. 2, ESA Publ. WPP-306), Venice, Italy, September 21–25, 2009.
- Swenson, M. S., & Niiler, P. P. (1996). Statistical analysis of the surface circulation of the California Current. *Journal of Geophysical Research*, *101*, 22631–22645.
- Zhurbas, V. M., & Oh, I. (2003). Lateral diffusivity and Lagrangian scales in the Pacific Ocean as derived from drifter data. *Journal of Geophysical Research*, *108*(C5), 3141. <https://doi.org/10.1029/2002JC001596>